

Downscaling of fracture energy during brittle creep experiments

O. Lengliné,¹ J. Schmittbuhl,¹ J. E. Elkhoury,² J.-P. Ampuero,² R. Toussaint,¹
and K. J. Måløy³

Received 25 October 2010; revised 22 May 2011; accepted 6 June 2011; published 27 August 2011.

[1] We present mode I brittle creep fracture experiments along fracture surfaces that contain strength heterogeneities. Our observations provide a link between smooth macroscopic time-dependent failure and intermittent microscopic stress-dependent processes. We find the large-scale response of slow-propagating subcritical cracks to be well described by an Arrhenius law that relates the fracture speed to the energy release rate. At the microscopic scale, high-resolution optical imaging of the transparent material used (PMMA) allows detailed description of the fracture front. This reveals a local competition between subcritical and critical propagation (pseudo stick-slip front advances) independently of loading rates. Moreover, we show that the local geometry of the crack front is self-affine and the local crack front velocity is power law distributed. We estimate the local fracture energy distribution by combining high-resolution measurements of the crack front geometry and an elastic line fracture model. We show that the average local fracture energy is significantly larger than the value derived from a macroscopic energy balance. This suggests that homogenization of the fracture energy is not straightforward and should be taken cautiously. Finally, we discuss the implications of our results in the context of fault mechanics.

Citation: Lengliné, O., J. Schmittbuhl, J. E. Elkhoury, J.-P. Ampuero, R. Toussaint, and K. J. Måløy (2011), Downscaling of fracture energy during brittle creep experiments, *J. Geophys. Res.*, 116, B08215, doi:10.1029/2010JB008059.

1. Introduction

[2] Heterogeneities in geological media have a strong impact on deformation processes in Earth's crust that are difficult to assess. Indeed, deformation is often multiscaled due to numerous local rheological variations (e.g., variability of rocks, mineralogy) and geometrical discontinuities (e.g., faults). These discontinuities are themselves often characterized by complex morphologies that lead to local stress concentrations [Okubo and Aki, 1987; Schmittbuhl *et al.*, 2006]. Microstructures like grains, cracks and mineral assemblage also contribute to the inhomogeneity of rock structures [Scholz, 2002; Paterson and Wong, 2005].

[3] Measurements of large-scale crustal deformation, usually done at the Earth surface, e.g., by GPS and InSAR [Blewitt, 2007; Simons and Rosen, 2007], allow limited constraints on the deformation at small scales, in particular at depth. Measurements in laboratory rock mechanics experiments suffer from the same limitations as sensors are located at the surface of rock specimens. Macroscopic information averaged over the sample size might be different from direct observations at the smaller scales at

which the physical mechanism responsible for the deformation is at play.

[4] Creep of faults and rocks produces smooth and continuous deformation when recorded at the system size, at large scales along faults [e.g., Titus *et al.*, 2006] and at small scales during creep laboratory tests [Heap *et al.*, 2009]. However, the presence of microearthquakes and transient deformation in creeping faults [Lengliné and Marsan, 2009] and acoustic emission (AE) in laboratory experiments [Lei *et al.*, 2000; Heap *et al.*, 2009] suggest that the deformation process is more intermittent and distributed over a wide range of velocities. The deformation induced by microearthquakes is generally not significant, although damage-related inelastic deformation contributes to the global deformation [Wang *et al.*, 2010].

[5] The differences in behavior between macroscopic and microscopic deformations highlight the importance of analyzing the physical processes at local scales at which observations can unambiguously be linked to a given mechanism. Moreover these differences question homogenization procedures, i.e., the upscaling of physical parameters from microscopic to macroscopic scales. The focus of our study is the relation between macroscopic smooth creep deformation and microscopic complex intermittent dynamics during crack propagation experiments. We address the link between macroscopic and microscopic scales where local strength heterogeneities are important.

[6] Creep deformation results from subcritical crack growth mechanisms and plays a significant role in time-

¹Institut de Physique du Globe de Strasbourg, IPGS, UMR 7516, CNRS, Université de Strasbourg, Strasbourg, France.

²Division of Geological and Planetary Sciences, California Institute of Technology, Pasadena, California, USA.

³Department of Physics, University of Oslo, Oslo, Norway.

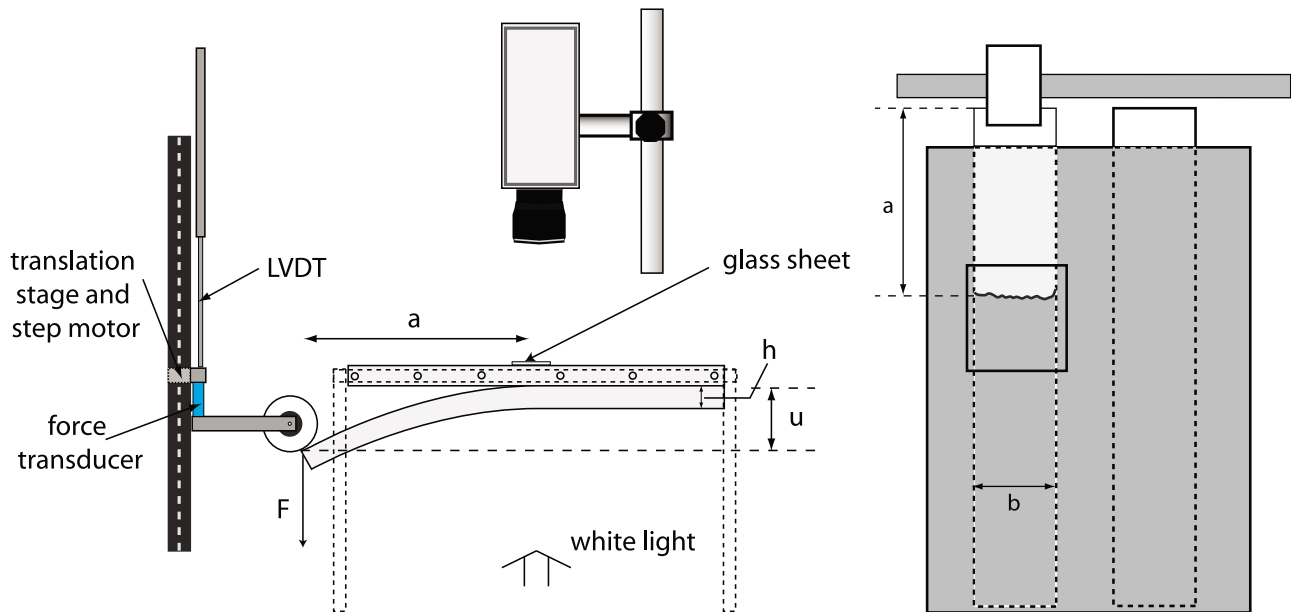


Figure 1. (left) Side view and (right) top view of the experimental setup. A stiff aluminum frame is attached to the upper PMMA plate. The bottom plate is separated from the upper one using a loading force F applied by a rod connected to a stepping motor. The load causes a deflection u of the bottom plate and the propagation of a mode 1 crack. The crack front is located at distance \bar{a} from the free end. The front advance is monitored by a high-speed camera set in vertical position, perpendicular to the crack plane. Lower plate height and width are noted h and b respectively.

dependent failure of rocks [Atkinson, 1984]. Among the numerous models of creep, the brittle creep model results from time-dependent microfracturing at the crack tip [Scholz, 1968a]. The smooth large-scale response in this model is a statistical response of a complex population of interacting microcracks [Scholz, 2002; Lockner, 1993; Baud and Meredith, 1997]. The time dependence might result from chemical processes like corrosive mechanisms. In particular, rocks feature a strong action of water on Si-O bonds. For polymers or metals, lateral motion of atomic kinks along the crack front, microplasticity or diffusion induce strength variation in time [Lawn, 1975; Atkinson and Meredith, 1987a]. This time dependence of slow kinetic crack propagation is usually well represented by a thermally activated mechanism where the strain rate obeys an Arrhenius law dependent on the energy release rate G (i.e., the energy available to drive the crack per unit area) [Lawn, 1993]. In this approach, the crack growth is directly influenced by environmental factors (applied stress, temperature, chemical concentrations) that affect the free energy, and thus the energy barrier, via numerous competing mechanisms like stress corrosion, diffusion, dissolution, plasticity and thermal effects [Atkinson and Meredith, 1987a; Lawn, 1993]. Experimentally, several empirical relations have been often reported to divide the slow crack propagation in three main characteristic regimes [Freiman, 1984]: (1) at very slow velocity, external variables are dominant and result in an increasing speed of crack growth with increasing G ; (2) a weak stress sensitive regime follows where transport is limiting, and (3) at higher stress crack growth kinetics is little influenced by environment.

[7] The energy release rate G is thus of primary importance when studying the creep mechanism and its scaling effect. G is often associated with a critical energy release rate G_c defined from the Griffith energy balance concept: the energy release rate equals the energy available to drive the crack per unit area $G = G_c$. Such fracture energy criterion is relevant to many geological processes like fault rupture or dike propagation [e.g., Rice and Simons, 1976; Rubin, 1993]. Estimation of G_c is difficult and relies on laboratory rock experiments [Wong, 1982] or earthquake rupture modeling using recorded waveforms or geological observations. Most measurements of the fracture energy are associated with a macroscopic quantity defined as a system size representative value, hence ignoring all fluctuations of G_c present at smaller scales. Here, we examine the relation between the macroscopic quantity and the smaller-scale variations in G_c . We do not investigate dynamic rupture (e.g., earthquakes) but slow, creeping fractures. This slow regime is relevant to many geophysical phenomena such as earthquake nucleation [Bouchon et al., 2011], slow slip events and postseismic slip [e.g., Das and Scholz, 1981].

[8] We present a series of quasi-static mode 1 fracture experiments performed on an experimental setting introduced by Schmittbuhl and Måløy [1997], Delaplace et al. [1999], and Grob et al. [2009]. The system allows to track a propagating crack in a brittle heterogeneous medium. We use samples of polymethylmethacrylate (PMMA), which, contrary to polycrystalline rocks, are transparent and allow for direct observation of crack deformation at the scale of the heterogeneities. The high temporal and spatial resolution of the experiment provides detailed information on

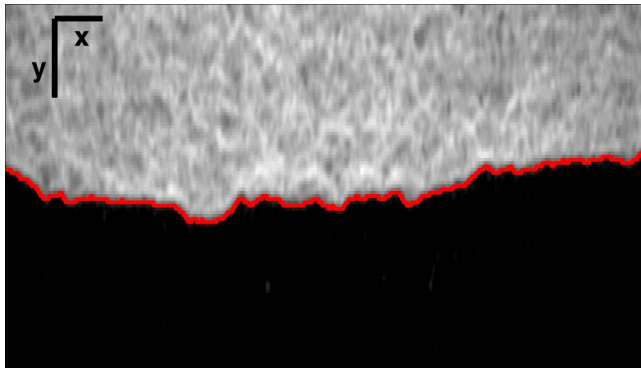


Figure 2. Zoom on the crack front displaying the difference between an image at the onset of the experiment and the current image of the front. During the experiment the crack front propagates from the top to bottom. The bright area marks the zone which is already cracked while in the dark area the two plates are still in contact (i.e., uncracked). The front line $a(x, t)$ is superimposed on the image as a red line. Scales are provided by two black segments which are 1 mm and 0.5 mm long respectively in the x and y directions.

the deformation process induced by the crack at the microscopic scale.

[9] We first present the macroscopic behavior of the fracture and an estimation of the relationship between fracture energy and average fracture velocity at the sample scale [Scholz, 1968a]. The brittle creep propagation of the crack is characterized by an intermittent dynamics at the microscopic scale and is well modeled by an activation energy mechanism. Then, we present the microscopic behavior of the fracture front roughness, the local fracture velocity and the local fluctuations of the energy release rate along the crack front line. The microscopic distribution of fracture energies spreads over a wide range and is directly linked to the disordered morphology of the interface. The fracture energy determined at the local scale is on average higher than the fracture energy computed at the global scale. This highlights the importance of local defects in controlling the rupture process in heterogeneous media. It also suggests that homogenization of the fracture energy is not straightforward and should be taken cautiously.

2. Experimental Setup

2.1. Sample Preparation

[10] We use two transparent PMMA plates of dimensions $20 \times 10 \times 1.0$ cm and $23 \times 2.8 \times 0.5$ cm (Figure 1). First, we sand blast one surface of the narrow plate with glass beads of diameter $\phi \in [180-300]$ μm . We clean the blasted plate to remove any electrically attached glass beads. Then we assemble the two plates in a stiff metallic loading cell with the blasted surface facing a surface of the larger plate. Finally, we impose an homogeneous normal load on the assembled plates and heat the loaded sample at 190°C for 45 minutes to anneal the plates. The thermal annealing produces a weak cohesive interface along which the sample breaks in mode I. The sand blasting introduces the random roughness of the plate surface that controls the local strength along the weak interface. It also induces microstructures at the plate

surface which make the sample opaque, but the newly formed block, after annealing, recovers its transparency since the contrast of the refraction index along the interface disappears.

[11] We choose PMMA in our experiment because (1) it is easy to handle and has a high transparency adequate for optical imaging, (2) its low Young modulus (3.2 GPa) allows fine tuning of small stress changes under imposed deformation, and (3) its surface energy, substantially larger than that of glass [Brace and Walsh, 1962; Katsamanis and Delides, 1988], limits the propagation of cracks at low applied stress. These combined properties enable a better control of the experimental system. Another advantage of PMMA compared to glass is its lower melting point which allows the welding of the PMMA plates at a much lower temperature and accordingly in an oven with a better temperature monitoring. In addition to these technical motivations, PMMA exhibits viscoelastic behavior. It is brittle at short time scales and semibrittle or even plastic at longer times. Macroscopically this long time scale regime is described by a ductile rheology. PMMA shows a time-temperature equivalence which is a very nice property for addressing either high temperature processes or very long term evolution. This richness of the PMMA rheology enables the observation of a mixed rupture regime macroscopically. It provides an attractive analogy for the study of numerous time-dependent mechanisms in the Earth's crust as those originating at the brittle-ductile transition. However, natural materials are generally very disordered at all scales due to the presence of microcracks, grains, pores and different minerals [Bean, 1996] that may increase the energy absorbed in the damage zone. Our PMMA material does not exhibit such strong disorder, and consequently the expected energy consumed around the crack tip by local plastic deformations is reduced.

2.2. Acquisition and Image Processing

[12] Once the sample is ready, we clamp the widest PMMA plate to a stiff aluminum frame. A stepping motor applies the loading over the top side of the narrow plate in a direction normal to the plate interface (Figure 1). We measure the vertical displacement of the loading point with a linear variable differential transformer (LVDT) and the loading force by an STC 1205 traction/compression transducer. Displacement and force are measured with a resolution of 1.3 μm and 2.4×10^{-3} N respectively. The vertical displacement imposed on the narrower plate induces stable propagation of a mode I planar fracture along the prescribed weak interface. We monitor the fracture front propagation using a fast optical camera (CamRecord 600) with up to 1000 fps. Images have a maximum dimension of 1024×1280 pixels and sample resolution is ~ 20 $\mu\text{m}/\text{pixel}$. For some experiments, we use a slow speed camera (Nikon D700) with up to 5 fps to follow the progression of the average front position over long time scales (Figure 1).

[13] Optical images of the interfacial mode I rupture show dark and bright regions respectively corresponding to open crack and unbroken parts of the sample (Figure 2). Image processing determines the transition between dark and bright areas that defines the fracture front. We first compute the difference between each image and the first image of the experiment. The image difference highlights the fracture front while removing permanent artifacts. Then, gray scale images are transformed into black and white images according

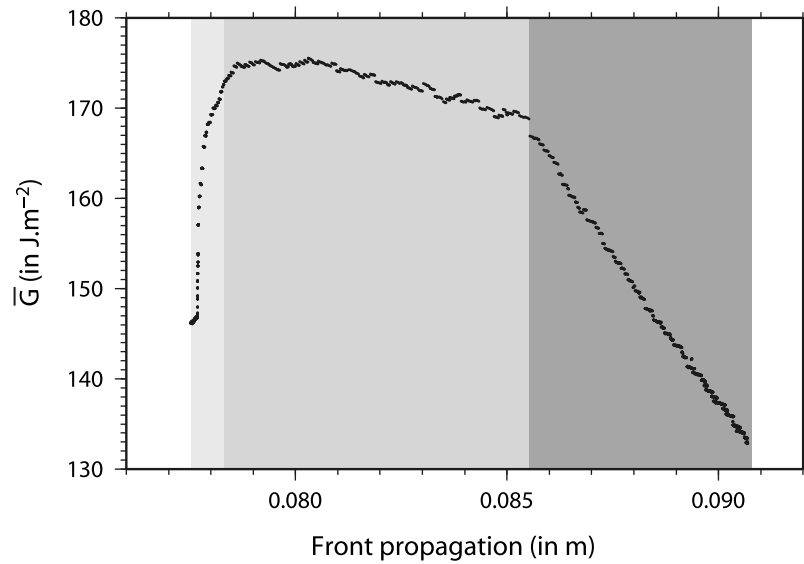


Figure 3. Evolution of \bar{G} during a mode 1 fracture experiment as a function of the crack front position. During this experiment, the sample is loaded at a constant speed. The front starts to move slowly and \bar{G} increases (light gray area) up to a nearly constant value when the crack front velocity reaches a steady state value (gray area). The loading point position is finally set to a constant value and \bar{G} decreases (dark gray area) before the loading point moves back to its initial position at the end of the experiment (in a part of the curve not displayed here).

to a gray level threshold separating bright and dark regions. Then, we compute the gradient in the direction of front propagation to highlight the transition zone. We finally extract connected pixels from the gradient images that correspond to the front position $a(x, t)$ (Figure 2). The front propagates along the y axis with the origin defined at the load point and is positive in the sense of crack propagation. The x axis is perpendicular to y and defines the coordinate of a point along the front (see *Måløy et al.* [2006] and *Grob et al.* [2009] for details).

2.3. Loading Procedure

[14] The loading rate is constant during an experiment but different among the experiments, ranging from 6 $\mu\text{m/s}$ to 300 $\mu\text{m/s}$. The crack advance for each experiment is on the order of 1 cm. We imposed a small transient load in one of the experiments. In several experiments we set the loading velocity to zero during the last stage to explore the fracture propagation under a fixed load point displacement (i.e., relaxation test). Here the average crack front velocity ranges from zero, at rupture initiation, to hundreds of $\mu\text{m/s}$. The rupture velocity in all experiments is much lower than the Rayleigh wave speed of the PMMA ($V_r \sim 1.7 \times 10^9 \mu\text{m/s}$).

3. Macroscopic Behavior

3.1. Energy Release Rate Evolution

[15] The macroscopic mechanical energy release rate during mode 1 crack propagation \bar{G} is related to the total strain energy U stored in the system by [Lawn, 1993]

$$\bar{G}(t) = -\frac{1}{b} \frac{dU(t)}{d\bar{a}(t)}, \quad (1)$$

where b is the plate width (Figure 1) and $\bar{a}(t)$ is the average position of the front, i.e., the spatial average of each profile

$a(x, t)$. Owing to the geometry of our setup, \bar{G} can be estimated by beam theory. In the approximation of small, purely elastic deformation and neglecting the weight of the plate, small compared to the loading force, the force F and load point displacement u (the deflection at the free end of the beam), are related by [Lawn, 1993]

$$F = \frac{E b h^3}{4 \bar{a}^3} u, \quad (2)$$

where E is the Young's modulus and h the height of the lower PMMA plate. We observe a linear relation between the observed average front position as a function of the predicted position (i.e., $[u/F]^{1/3}$) that proves the validity of the elastic beam theory applied to our experiments (equation (2)). The energy stored in the plate is

$$U = \frac{uF}{2}. \quad (3)$$

Combining equations (1) to (3) we obtain

$$\bar{G} = \frac{3 E h^3}{8} \frac{u^2}{\bar{a}^4}. \quad (4)$$

This is the usual expression of the energy release rate for a simple cantilever beam under imposed displacement and neglecting mode 2 loading [Lawn, 1993]. Equation (4) can be written in terms of the observables F , u and \bar{a} as

$$\bar{G} = \frac{3 F u}{2 b \bar{a}} \quad (5)$$

using equation (2). We prefer expression (5) instead of (4) because it involves measured variables raised to lower powers, which reduces the uncertainties. We track the evo-

Table 1. Macroscopic Energy Release Rate Determined for All Seven Experiments Performed With the Fast Speed Camera^a

Experiment	\bar{G}_c	$\langle \bar{G} \rangle$	\bar{G}_{area}
1	174	148	144
2	122	118	126
3	153	140	123
4	147	142	113
5	182	173	167
6	130	122	115
7	190	182	159

^aThe values of the fracture energies \bar{G}_c are obtained by taking the maximum of \bar{G} computed from equation (5) for each experiment. We also report the mean energy release rates during the crack propagation obtained by the beam theory ($\langle \bar{G} \rangle$) and by integration under the deflection-force space \bar{G}_{area} . All values are in $J \cdot m^{-2}$.

lution of \bar{G} (equation (5)) during crack propagation as F , u and a are continuously monitored (Figure 3).

[16] The crack propagates at steady speed when the macroscopic energy release rate \bar{G} reaches a plateau that defines the macroscopic fracture energy \bar{G}_c (Figure 3), consistently with a macroscopic Griffith equilibrium. \bar{G}_c is in the range $122 J \cdot m^{-2}$ – $190 J \cdot m^{-2}$ for the set of experiments presented here. The fracture front also propagates during the relaxation regime (final stage of the experiment in Figure 3) with decreasing velocity. This propagation happens while $\bar{G} < \bar{G}_c$, which is not predicted by the Griffith theory with time-independent \bar{G}_c .

[17] We also estimate the global energy release rate directly from equation (1). The strain energy loss due to the crack propagation is the area ΔA defined in the deflection-force ($u - F$) space, between the loading and unloading curves. We numerically integrate ΔA and divide it by the crack length increase $\Delta \bar{a}$ and the plate width b . This approach provides an independent estimate \bar{G}_{area} and validates the beam approach employed above under the assumption of a constant energy release rate during the entire crack propagation regime. We report the energy release rates and fracture energies for a subset of experiments in Table 1. Although some discrepancies exist between the two methods, we observe that a simple elastic beam model is appropriate to first order. Typical uncertainties in G are on the order of 7.5% given the uncertainties in F , u , b and a (typical values are $F = 30 \pm 0.2 N$, $u = 10^{-2} \pm 10^{-6} m$, $b = 2.8 \pm 0.2 cm$ and $\bar{a} = 10 \pm 0.2 cm$). This relative uncertainty in \bar{G} partially accounts for the small differences observed between the two methods used for its calculation. However, discrepancies might also be due to viscoelastic effects and yielding at the crack tip which contribute to energy loss during crack propagation but are neglected in our calculation. These effects are unfortunately difficult to estimate and we did not attempt to quantify their importance. It is worth noting that fracture energies in PMMA are of the same order of magnitude as those for rocks in mode I experiments at room conditions [Atkinson and Meredith, 1987b] and significantly higher than those for minerals [Scholz, 2002].

3.2. Brittle Creep Crack Propagation Model

[18] The crack propagation we observe at $\bar{G} < \bar{G}_c$ is not accounted for by the Griffith criterion (Figure 3). This is particularly pronounced towards the end of experiments where the loading displacement is fixed, which induces

crack propagation at decreasing speed while \bar{G} also decreases. Many mechanisms produce time-dependent sub-critical crack advance where the velocity v follows an Arrhenius law [Wiederhorn and Bolz, 1970]

$$v(G) = v_o \exp \left[\frac{\beta G - E'}{RT} \right], \quad (6)$$

where G is the energy release rate, E' is an energy barrier, R is the universal gas constant and T is the temperature. β and v_o are material-dependent empirical constants and the energy release rate G is directly linked to the stress intensity factor K by $K = \sqrt{G E}$ in plane stress.

[19] We consider our fracture interface as a set of discrete sites of varying energy release rate along which the crack front line is pinned [Scholz, 1968b]. We describe the energy release rate by a probability density function $f(G, \bar{G})$. It is the probability of a point along the front line to have an energy release rate G given an average energy release rate \bar{G} along the front. The probability distribution arises from the interplay between local toughness fluctuations on the interface and elastic interactions among sites of the front line. Equation (6) is understood as the local propagation criterion. It can be viewed as proportional to the inverse time to failure for a site locally loaded by a constant energy release rate G . The average crack front velocity $d\bar{a}/dt$ is defined by

$$\frac{d\bar{a}}{dt} = \int_{G=-\infty}^{+\infty} f(G, \bar{G}) v(G) dG. \quad (7)$$

[20] We assume a normal distribution for $f(G, \bar{G})$ with mean \bar{G} and standard deviation σ_G [Scholz, 1968a]:

$$\frac{d\bar{a}}{dt} = \int_{-\infty}^{+\infty} \frac{v_o}{\sqrt{2\pi}\sigma_G} \exp \left[-\frac{1}{2} \left(\frac{G - \bar{G}}{\sigma_G} \right)^2 + \frac{\beta G - E'}{RT} \right] dG, \quad (8)$$

which integrates to

$$\frac{d\bar{a}}{dt} = v_o \exp \left[\frac{\beta \bar{G} - E'}{RT} + \frac{\beta^2 \sigma_G^2}{2R^2 T^2} \right] = \bar{v}_o \exp \left[\frac{\beta}{RT} \bar{G} \right], \quad (9)$$

where $\bar{v}_o = v_o \exp \left[\frac{\beta^2 \sigma_G^2}{2R^2 T^2} - \frac{E'}{RT} \right]$. Equation (9) plainly shows that the evolution of the crack front velocity at the macroscopic scale is described by the same functional form as in the microscopic scale (equation (6)). Equation (9) implies $\bar{v} \propto \exp(\bar{G})$ independently of the loading conditions, extending its validity to the entire duration of the experiment. Equation (9) also reproduces the average evolution of the crack speed as a function of the macroscopic energy release rate \bar{G} (Figure 4). It is also applicable when $du/dt = 0$. Since $\bar{a}(t)$ is small in the creeping regime, we use a first-order expansion around the initial position \bar{a}_0 :

$$\bar{G}(\bar{a}) = \bar{G}_0 + \frac{d\bar{G}(\bar{a}_0)}{d\bar{a}} (\bar{a} - \bar{a}_0), \quad (10)$$

where \bar{a}_0 is the average position of the front at the onset of the creeping regime and $\bar{G}_0 = \bar{G}(\bar{a}_0)$. Substituting into (9), we get

$$\frac{d\bar{a}}{dt} = \bar{v}'_o \exp[-C_0 \bar{a}], \quad (11)$$

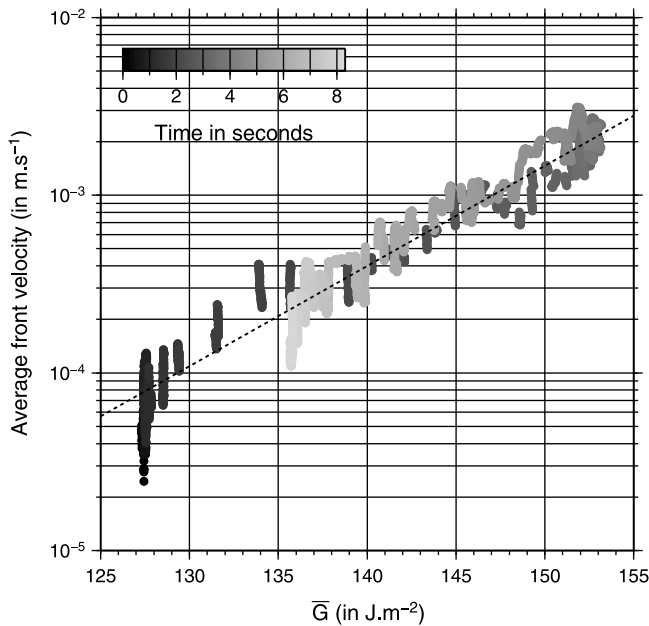


Figure 4. Variation of the average crack velocity $d\bar{a}/dt$ as a function of the average energy release rate \bar{G} for an experiment conducted with the high-speed camera. The gray scale refers to the time since the start of the recording. During the entire crack propagation, from the initiation phase up to the relaxation phase, the best fit using equation (6), displayed as a dashed line, provides a good description of the data. It suggests that the crack propagation is a process driven by time-dependent brittle creep.

where $\bar{v}'_0 = \bar{v}_0 \cdot \exp(5\beta \bar{G}_0/RT)$ and $C_0 = 4\beta \bar{G}_0/RT\bar{a}_0$. After integration we get

$$\bar{a}(t) - \bar{a}_0 = \frac{1}{C_0} \ln[C_0 \bar{v}'_0(t - t_0) + \exp(C_0)], \quad (12)$$

where t_0 is the time at the onset of the creeping regime.

[21] We also investigate the prediction of the model in the case $du/dt \neq 0$. When the front reaches a steady state regime, the crack propagates with $\bar{G} = \text{constant}$. This condition is similar to the Griffith energy criterion. A propagation with a constant energy release rate is described from equation (4) by

$$\bar{G} = \frac{u^2}{\bar{a}^4} \frac{3Eh^3}{8} \quad \text{and} \quad a(u) = \sqrt{u} \left(\frac{3Eh^3}{8\bar{G}} \right)^{1/4}. \quad (13)$$

Equation (12) provides a good description of the macroscopic evolution of the crack front in the relaxation regime (Figure 5, bottom) and equation (13) provides a good description in the forced regime (Figure 5, top). The macroscopic evolution of the front advance is well reproduced by a subcritical crack growth mechanism (Figures 4 and 5) that explains the propagation of the crack even for an energy release rate (or similarly the stress intensity factor) lower than the interface fracture energy (or similarly the toughness). It is also valid even when the front is propagating at a

constant speed. In order to supplement our estimation of the fracture energy, next we present a procedure to estimate G at the local scale.

4. Microscopic Behavior

4.1. Scaling of the Fracture Front

[22] So far, we only considered straight crack fronts. These are expected if the toughness is uniform along the interface. However, departures from the straight front geometry suggest lateral variation of material resistance due to the sand blasting procedure applied during the sample preparation (Figure 6). The morphology of propagating interfacial cracks has been intensely studied [Schmittbuhl and Måløy, 1997; Delaplace et al., 1999] and reproduced numerically [Schmittbuhl et al., 2003a]. The in-plane morphology of crack fronts is self-affine and can be characterized by a roughness exponent. We show that a similar scaling of the fracture front morphology exists in our experiments. The Fourier transform of each front line, for a given experiment, is computed after detrending and tapering the original profile $a(x, t)$. We then obtain the average power spectrum representative of all fronts in this experiment (Figure 6). We observe a power law decay of the power spectrum in agreement with a self-affine morphology and the roughness exponent is in agreement with previously reported values ($H = 0.6$) [Santucci et al., 2010]. Variable geometry of the crack front line suggests that heterogeneities over the interface should be taken into account when evaluating the fracture energy.

4.2. Distribution of Local Velocities

[23] The waiting time spent by the crack front at each local site is power law distributed [Måløy et al., 2006]. The intermittent dynamics at the microscopic scale is also indirectly evidenced in rocks during creep tests [e.g., Heap et al., 2009]. The recording of acoustic emissions during a slow macroscopic deformation suggests that at the local scale the deformation is distributed over a wide range of velocities. Figure 7 shows, for two experiments, the probability density function (pdf) of v obtained by the procedure described by Måløy et al. [2006]. The broad distribution of local speeds, spanning more than 2 orders of magnitude, highlights the irregular nature of the fracturing process at the small scale.

4.3. Local Energy Release Rate

4.3.1. Nonstraight Front Geometry

[24] We follow a first-order analysis based on a perturbation method for nearly straight crack fronts, valid for small relative variations of the fracture energy [Gao and Rice, 1989]. This approach is valid in our experiments since front lines are straight at first order. Furthermore, the model adequately reproduces the morphology of experimentally propagating cracks, although a discrepancy in the value of the roughness exponent remains [Schmittbuhl et al., 2003a]. However, this approach ignores crack coalescence, which can play a role in redistributing stresses ahead of the crack front [Hansen and Schmittbuhl, 2003; Schmittbuhl et al., 2003b]. Here we assume that the elastic front line model represents the dominant process. The first-order

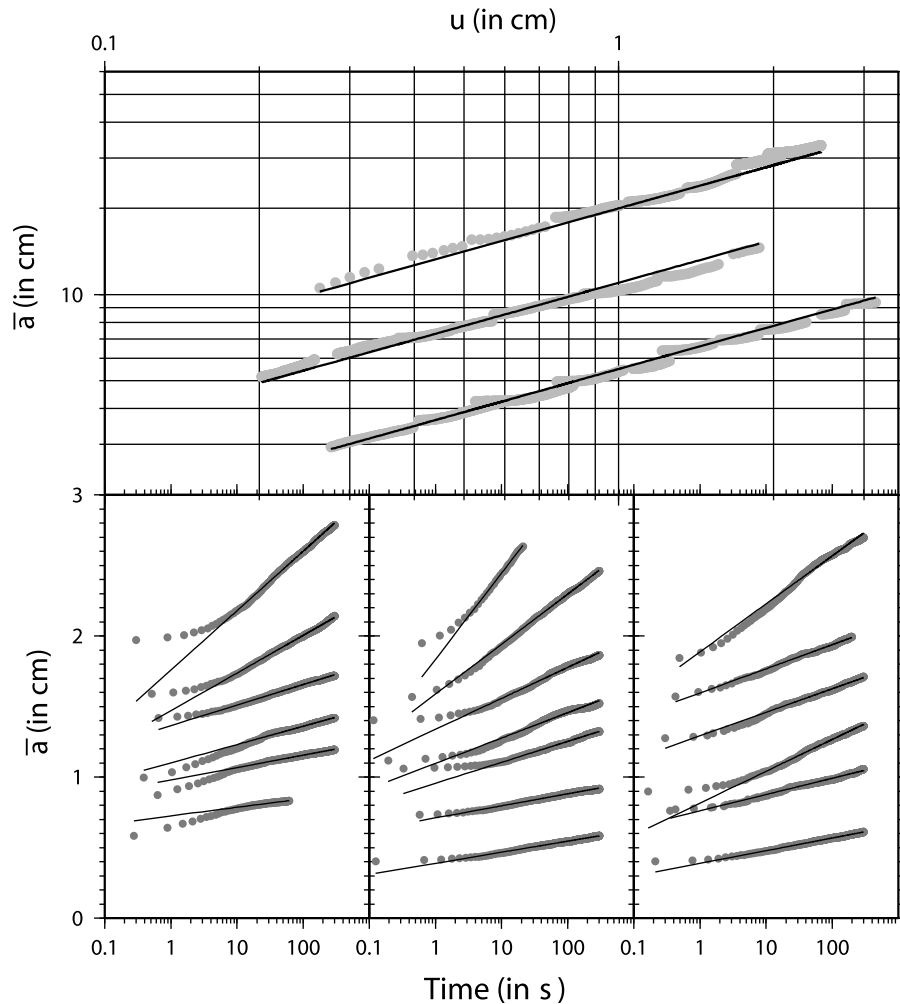


Figure 5. (top) Variation of the average crack front position \bar{a} as a function of the loading point displacement u . The gray points refer to data recorded from different samples. For each sample we carried out several experiments. The best fit using equation (13) is displayed as a black line for each sample. Crack front positions are shifted vertically for each sample in order to enhance the visibility. (bottom) Evolution of the average front position \bar{a} during the relaxation regime (gray dots). The x axis is the time after we stopped the loading. For each experiment, the best fit using equation (12) is displayed as a black line. A good match of the fitted line to the data is observed after several seconds which marks a transition period from the previous regime. Each of the three bottom images represents a different sample. For each experiment, the vertical axis is shifted in order to enhance visibility.

approximation of the energy release rate of an almost straight crack is [Gao and Rice, 1989]

$$G(x_i, t_k) = \bar{G}(t_k)(1 + \gamma(x_i, t_k)) \quad (14)$$

for a given front at time t_k . $\bar{G}(t_k)$ is the energy release rate computed from the average front position at time t_k and $\gamma(x_i, t_k)$ is the contribution from elastic interactions due to local fluctuations of the front position given by

$$\gamma(x, t) = \frac{1}{\pi} \mathcal{P}\mathcal{V} \int_{-\infty}^{+\infty} \frac{a(x', t) - a(x, t)}{(x - x')^2} dx', \quad (15)$$

where $\mathcal{P}\mathcal{V}$ denotes the principal value. This expression is the Hilbert transform of the local slope of the front [Ampuero and Rubin, 2008], which explains why small-

scale variations in the $\gamma(x)$ profile are larger than in the $a(x)$ profile. The discretized version of equation (15) is

$$\gamma(x_i, t_k) = \frac{1}{\pi} \sum_{j=-l/2, j \neq i}^{l/2} \frac{a(x_j, t_k) - a(x_i, t_k)}{(x_j - x_i)^2} . dl, \quad (16)$$

where dl is the width of a pixel and l is the width of the picture. A small error may arise in the determination of γ for points close to the edge of the images of the fracture front. Since the decay of the elastic kernel with distance is fast ($\propto 1/x^2$), the loss of information at the edge only affects a small region near the edge of the picture. The computation of γ , as presented in equation (16), assumes a half plane crack in an infinite body. If the finite height of the plate is taken into account, the elastic kernel transitions from the $1/x^2$

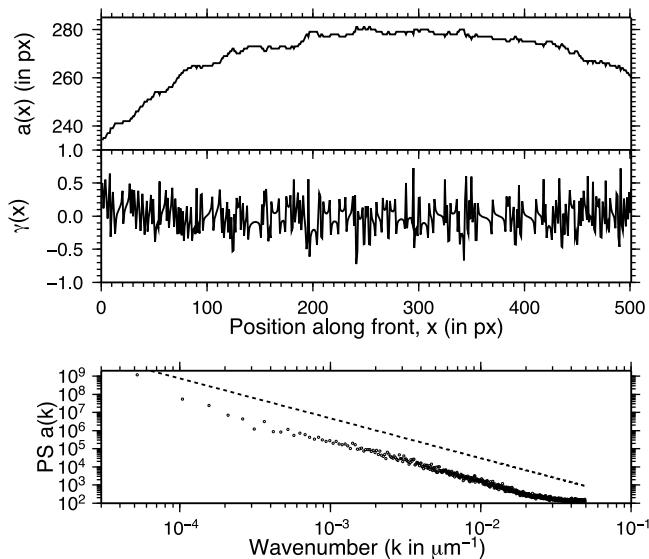


Figure 6. (top) Example of front position $a(x)$ extracted from a picture captured with the high-speed camera. Distances are in pixels and the size of a pixel is $\sim 21 \mu\text{m}$. The difference between the less advanced and the farthest advanced point on the front is slightly less than 1 mm whereas the front length is ~ 1.1 cm. (middle) The γ values corresponding to the front line displayed above and computed using equation (16). We observe sharp fluctuations of γ which are correlated with local variations of the slope of the front $a(x)$. (bottom) Averaged power spectrum (PS) of the front morphology over all fronts extracted during an experiment. We observe a clear power law decay of the PS which shows the presence of fluctuations of $a(x, t)$ at all spatial scales and is representative of the self-affine nature of the crack front morphology. The dashed line indicates a power law decay function with an exponent of -2.2 , consistent with a roughness exponent $H = 0.6$.

behavior of equation (15) to a faster (exponential) decay at distances x larger than the plate height. We calculate the local value of γ at the middle of a front line in order to quantify the impact of the truncation and the finite height. We progressively extend the bounds of the summation up to $l/2$. Two different front lines originating from two different experiments are processed in this way to represent the typical convergence of γ as a function of the integration range. We observe that $\sim 90\%$ of the final estimate of γ is recovered in the first 100 pixels which corresponds to a dimension of 2 mm (Figure 8). This shows that γ is controlled by the closest neighboring sites. The infinite medium approach is valid since the length scale influencing the estimate of γ is smaller than all other dimensions of the plate. An example of a γ profile for a given front is shown in Figure 6.

4.3.2. 1-D Time Evolution

[25] The matrix $\gamma(x, t)$ represents normalized fluctuations of the energy release rate at any time and position along the front. The mean of the γ distribution, along a given front line, for a given image, is zero by definition. We track the evolution of $\gamma(x_0, t)$ for a particular position, x_0 , along the front (Figure 9). The local movement of the front $a(x_0, t)$

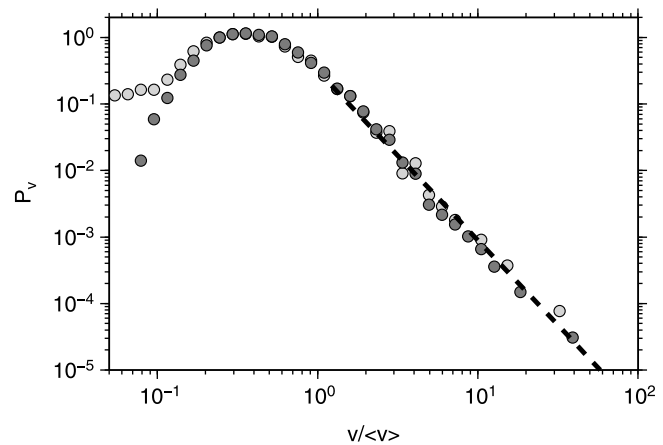


Figure 7. Probability density function of the local speed computed for two different experiments (light and dark gray circles). All velocities are normalized by the average crack propagation velocity in order to compare experiments. We clearly observe a power law decay of the pdf above $v/\langle v \rangle = 1$. The dashed line indicates a power law decay with exponent -2.55 as found by *Måløy et al.* [2006].

reveals potential correlations between the evolution of γ and local variations of a (Figure 9).

[26] The local motion of the front is not continuous but rather exhibits a stick-slip pattern with long resting periods followed by jumps of the front position (Figures 7 and 9). In contrast, the large-scale evolution of the average crack position is continuous.

4.3.3. 2-D Maps

[27] The energy release rate increases at pinned positions along the front line. This increase has two contributions: (1) a large-scale contribution from the external loading applied to the system (increase of the load point deflection) and (2) local contributions resulting from local elastic interaction due to the differential movement of neighboring points. As G increases, it rises the probability of the local site

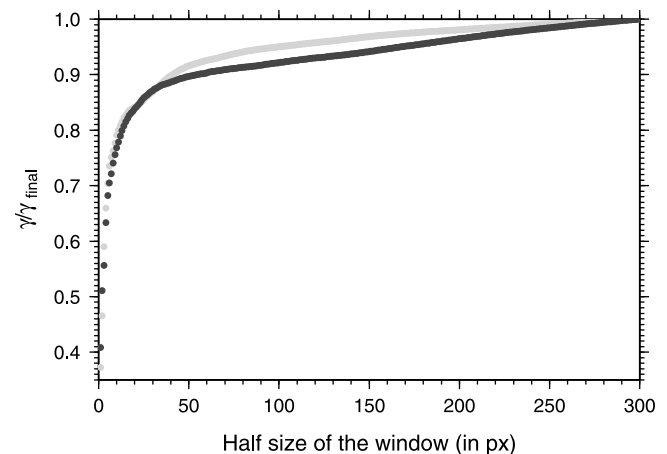


Figure 8. Convergence of γ to its final estimate as a function of the half size of the window used to compute it. This convergence is tested on two different front lines taken from two different experiments. Convergence is fast: $\sim 90\%$ of the final estimate of γ is recovered in the first 100 pixels (2 mm).

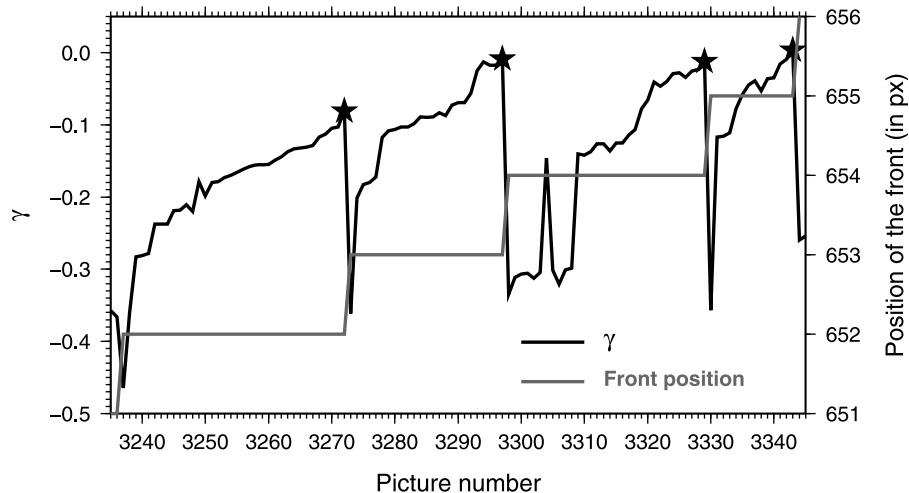


Figure 9. Evolution of γ (black line) and front position (gray line) for a given position along front and during ~ 8 s. Stars represent the last values of γ at a given front position and are defined as γ_c .

to fail in the next time interval as defined by equation (6). This probability increases until G reaches G_c , at which point the local site breaks. Accordingly, we define γ_c as the last value of γ just before a local variation of the front position and we estimate the fracture energy at this site as

$$G_c(x_i, a(x_i, t_k^*)) = \bar{G}(t_k^*) (1 + \gamma(x_i, a(x_i, t_k^*))), \quad (17)$$

where t_k^* is the time at which γ_c was reached. It is important to note that $\bar{G}(t_k^*)$ is obtained from the measurement of the average position of the front $\bar{a}(t_k^*)$. Any variation of γ taking place during the time interval between estimating γ_c and the local front advance is neglected. These microscopic estimates of the fracture energy are lower bounds, since there is a finite probability that the local site actually breaks with $G < G_c$ according to the Arrhenius model described earlier. In order to get an insight on collective processes that take place at the local scale during the crack propagation, we show two examples of a spatiotemporal map $\gamma(x, t)$ in Figure 10. These maps are subregions of the effectively recorded areas (both in time and space) taken from two different experiments representative of the two propagation regimes, at fixed loading point (relaxation regime) and constant loading rate respectively.

[28] Notable features emerging from Figure 10 are summarized below:

[29] 1. At a given time (horizontal line), only a few points are at $G = G_c$, and most points have $G < G_c$ for both forced ($\bar{G} = \bar{G}_c$) and relaxation regimes. Observation of the intermittent failure of local sites during slow crack propagation is a direct measurement of a brittle/creep behavior. As most of the sites along the front line are below G_c , the macroscopic estimate of fracture energy \bar{G}_c is an average among local values of G that are mainly below the critical state ($\bar{G} \neq \bar{G}_c$). Therefore, the macroscopic fracture energy is a lower estimate compared to the microscopic values.

[30] 2. Large collective failure events (numerous black points on the same horizontal line) corresponding to a burst of activity in a relatively short time interval occur at discrete periods. These fast local movements arise from a connected

set of unstable positions along the front. A burst of unstable positions appears when the local G is equal or higher than the fracture energy of all sites of the cluster. This scenario typically occurs after breaking a strong local asperity (high G_c value). The front then travels in a region with lower G_c up to a new arrest position that corresponds to the next accessible equilibrium position.

[31] 3. Despite very different average velocities and loading regimes, strong similarities exist between the patterns of the two maps. The main difference between the two loading regimes arises from the waiting time between each successive move of the front at a particular local site. Time intervals between two successive moves are much larger in the relaxation regime (frame rates in Figure 10 are 125 fps and 1000 fps for the relaxation and the forced regime respectively). The shorter time intervals observed in the forced regime are related to a higher loading rate at each local site.

4.4. Influence of Fluctuations in Toughness

4.4.1. Large-Scale Fluctuations

[32] The front geometry has a long wavelength curvature due to a large-scale variation of the fracture energy at the interface. The annealing condition in the sample during its preparation is not perfectly homogeneous. Transient heat diffusion from the sides of the plates to the center of the sample is possibly responsible for such curvature. As a consequence, edges of the plate have higher strength than the center. We used this large-scale curvature of the front line to infer the large-scale variation of the fracture energy along the x direction. The largest Fourier mode of the front is a single cosine function of the form $a(x) = A_0 + 2A_1 \cos(\pi x/b)$ where x is the coordinate along the front direction and b is the width of the plate [Gao and Rice, 1989]. Griffith criterion holds everywhere along the crack front (G very close to G_c), with G_c being the local fracture energy at each site. It follows from [Gao and Rice, 1989]

$$\sqrt{\bar{G}} = \sqrt{\bar{G}_0} \left[\frac{1}{A_0} - \frac{\pi}{L} \right] A_1, \quad (18)$$

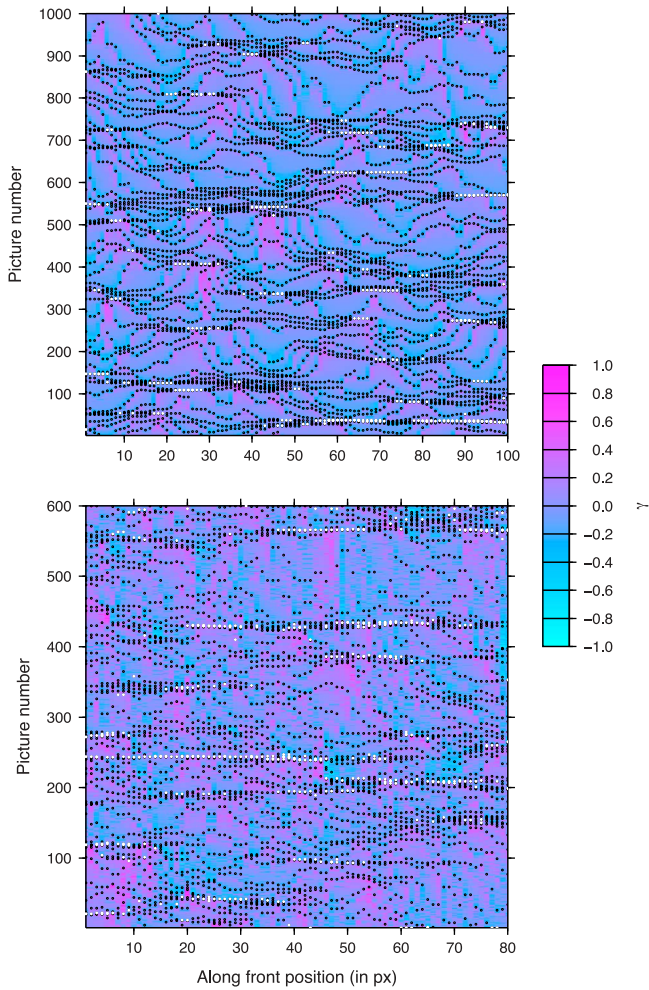


Figure 10. Zooms on a subspace of γ matrix obtained using equation (16) for two experiments recorded with the fast video camera at (top) 125 fps and (bottom) 1000 fps. Time axis is vertical and is oriented from bottom to top. Note that the time interval between two pictures is not the same for the two maps (8 s and 0.6 s). The top image is obtained while the front is relaxing (i.e., $u = \text{constant}$) while the bottom image was obtained while the front was propagating at constant velocity. Black dots correspond to last positions of the front before a local move and thus define G_c as expressed in equation (17). White dots correspond to estimation of G_c obtained from only one measure, thus reflecting the non-equilibrium position of the front at these locations.

where \tilde{G} and \tilde{G}_0 are the Fourier modes of order 1 and 0 respectively. The variation of fracture energy at long wavelength between the center of the plate and its border is

$$\frac{G_c^{\text{center}}}{G_c^{\text{border}}} \approx \left(\frac{b - \pi A_1}{b + \pi A_1} \right)^2 \quad (19)$$

for $A_0 \gg b/\pi$ which is the case for our experiments. As A_1 is on the order of several hundred of micrometers and b is ~ 2 cm, the long wavelength shape of the front is explained

by a variation of fracture energy along the plate on the order of 10%.

4.4.2. 2-D Toughness Fluctuations

[33] We estimate spatial maps of local fracture energies $G_c(x, a(x))$, i.e., everywhere along the interface, from equation (17) (Figure 11). The local fracture energy is broadly distributed over the range 18 to 395 J.m^{-2} , clearly expressing the heterogeneity of local fracture energies (Figure 11). Interface roughness δz is obtained from a broken sample, previously peeled off (Figure 11). The analyzed interface does not correspond to the same area where the G_c map was computed but the statistical properties of the interface morphology are assumed to be representative of the whole sample interface. The morphology of the interface was measured by a laser profilometer with spatial and vertical resolution of $10 \mu\text{m}$ and $\sim 1 \mu\text{m}$ respectively (Figure 11). Height fluctuations δz have a standard deviation of several of μm .

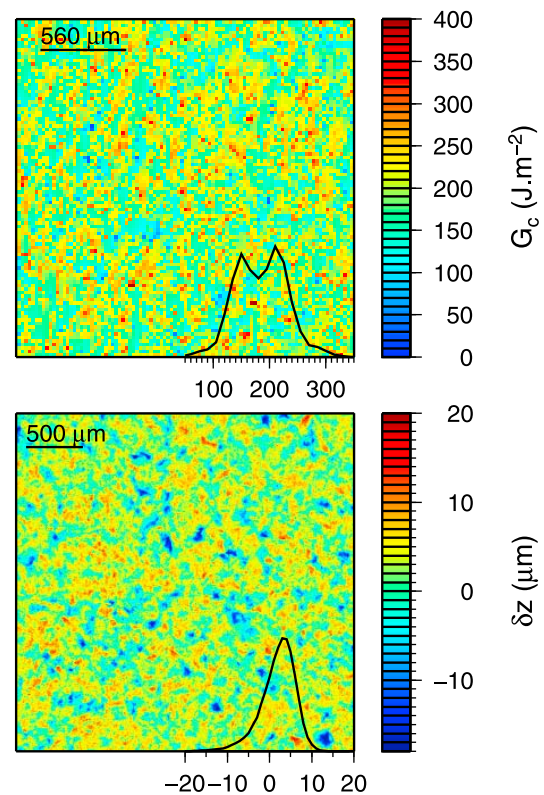


Figure 11. (top) Zoom on a map of local fracture energy G_c computed using equation (17). During this experiment the crack propagates from bottom to top. We clearly observe an heterogeneous distribution of G_c which appears as a random field although a correlation among sites can be identified. The few holes (3% of total number of pixels) that exist at some places in the map, because of a too low frame rate, have been filled by linear interpolation. The inset graph represents the distribution of fracture energy for all sites of the main picture. (bottom) Map of a sample interface morphology δz of a similar size to the one represented for the fracture energy. An heterogeneous distribution of δz is clearly visible with an amplitude of variation of several tens of micrometers. The inset graph represents the distribution of the interface height δz .

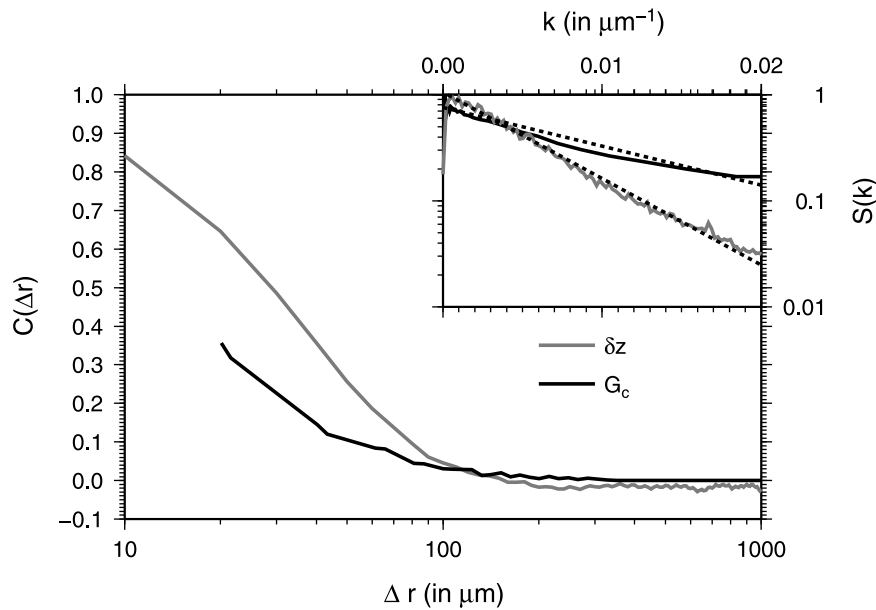


Figure 12. Averaged correlation functions $C(\Delta r)$ as a function of the distance Δr between two points along the interface. Correlations are averaged from stripes computed along the front direction and perpendicular to it. The gray line denotes the correlation function computed for the interface morphology whereas the black line represents the correlation functions of the fracture energy. The inset shows the two power spectra $S(k)$ from which correlation functions are computed. The best exponential fit for each function $S(k)$ is plotted as a dashed line. The correlation lengths inferred from these fits are $r_c = 188 \mu\text{m}$ and $84 \mu\text{m}$ for the height and fracture energy respectively. The values are in agreement with the lengths where the correlations functions $C(\Delta r)$ get uncorrelated.

[34] Local toughness variations arise from the squeezing of local asperities along the interface. We extract all profiles of G_c and δz along the front propagation direction and perpendicular to it. The power spectra $S(k)$ is averaged over the two in-plane directions for both the distributions of G_c and δz . The autocorrelation function $C(\Delta r)$ is then obtained as the inverse Fourier transform of the power spectrum:

$$C(\Delta r) = \int_{-\infty}^{\infty} S(k) e^{i2\pi k \Delta r} dk, \quad (20)$$

where k is the wavenumber. Figure 12 shows correlation functions of the fracture energy and the surface morphology along with their power spectra $S(k)$. The autocorrelation functions of G_c and δz decrease with distance (Figure 12). The decrease is faster for G_c than for δz . The power spectra shows an exponential form although we cannot exclude a model with power law decay associated with a cutoff length. An exponential of the form $S(k) \propto \exp(-k/k_c)$ is an adequate fit. The length scale $1/k_c$ is the correlation length, the distance beyond which the distribution becomes uncorrelated. For the front morphology we find $1/k_c \sim 188 \mu\text{m}$. The distribution of G_c is characterized by a smaller correlation length $\sim 84 \mu\text{m} \sim 4$ pixels. These cutoff length scales can also be appraised from the correlation functions as we observe that $C(\Delta r)$ gets around 0 above these distances. Although the cutoff length is not the same, the exponential decay is observed for both G_c and δz . The existence of a finite correlation length for G_c and δz does not necessarily imply that an approach using a representative element volume (REV)

could be valid at scales greater than this length scale. Long range interactions, owing to elastic forces applied over long distances results in an interplay between the toughness fluctuations and these elastic forces. This is well demonstrated by the self-affine nature of the crack front line observed previously (section 4.1).

5. Scaling of the Fracture Energy

[35] The observation that most points along the crack front have energy release rate $G < G_c$ indicates that the macroscopic estimate of the fracture energy $\overline{G_c}$ is different from the fracture energy at the local scale. We test this proposition by comparing G_c at the local and the global scales. In particular, we address whether the macroscopic toughness is a simple arithmetic average of the distribution of local toughness. In such a case, an homogenization procedure is quite straightforward and $G_c = \langle G_c \rangle$, i.e., the local variations of material resistance are simply scattered around the global value and the average of the distribution is equal to the global value. We calculate normalized distributions of G_c as well as global estimations of $\overline{G_c}$, obtained with equation (5) for each experiment (Figure 13). We only consider for the estimates of G_c those locations where the front was present during more than one time interval. The estimate involves only values at equilibrium positions and thus related to the interface property [Roux *et al.*, 2003]. We also calculate the normalized distribution of G computed from equation (14) (Figure 13). The distribution of local energy release rate is wide and is centered on the macroscopic estimate of the fracture energy. This is expected from

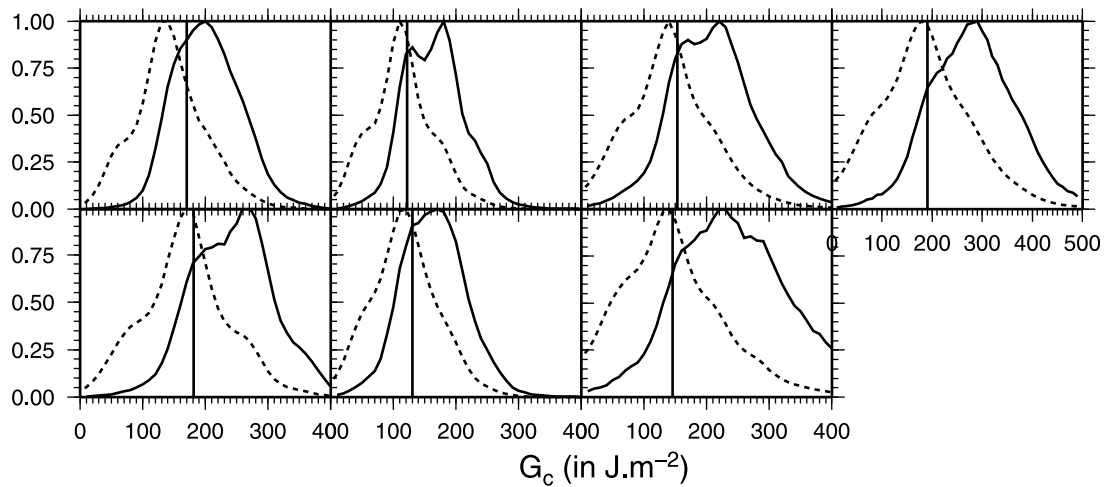


Figure 13. Distributions of G_c (black line), G (dash line) for all seven experiments carried with the fast video camera. The vertical black lines is the value of the macroscopic fracture energy \bar{G}_c . We systematically observe that the microscopic distribution of G_c is centered on higher value than their respective macroscopic estimates.

equation (14) and equation (16), because γ has zero mean. Accordingly, the distribution of G should be approximately centered on the global value \bar{G} , as observed. A more interesting feature emerges when analyzing the distribution of local fracture energy G_c (Figure 13). We clearly observe that the average of local fracture energy $\langle G_c \rangle$ is higher than the macroscopic estimate of the fracture energy \bar{G}_c . We recall that the macroscopic estimate of the fracture energy \bar{G}_c is defined as the maximum value of the \bar{G} reached during the crack propagation. Such higher values of G_c compared to \bar{G}_c are observed for all experiments and the distribution of G_c is systematically shifted to higher values compared to the global \bar{G}_c . This indicates that G_c samples the subset with the highest values of G . For a pinned position of the front, γ increases with time leading to higher values at the end of the time interval, just before the local advance of the front. Therefore, γ_c are on average higher than γ and the distribution of G_c is shifted towards higher values compared to G . It is worth noting that the shift to higher values, going from macroscale to microscale, does not depend of any particular choice of calculating \bar{G} . For example, equations (4) and (5) produce a similar shift of $\langle G_c \rangle$ compared to \bar{G}_c because G_c values are computed using \bar{G} from equation (14). The observed toughening effect at the microscopic scale is thus independent on a particular calculation of \bar{G} . The same argument is also valid when considering the variation of \bar{G} owing to the uncertainties of the parameters defining \bar{G} . Despite these uncertainties, local values of G_c will still be, on average, higher than \bar{G}_c . We note however that the amplitude of this toughening depends on the macroscopic value of the energy release rate.

[36] There are some known geophysical scaling problems where a simple arithmetic mean (average) is not relevant for an upscaling of the problem. For example, bulk permeability of a heterogeneous material is bounded from above by the arithmetic mean and below by the harmonic average [Zimmermann and Main, 2004]. Contrary to the case of the permeability, for which the Darcy's law allows to make the transition link between scales, an equivalent expression does

not exist in our problem. This prevents us to define the particular averaging procedure relevant in our system. Nevertheless, we test several forms of mean of our values of G_c . We compute the harmonic, the geometric and the arithmetic means of the microscopic distribution of fracture energy for each experiment. We observe for all experiments that all types of average are systematically overestimating the macroscopic value. This suggests that scaling effects are non trivial and related to the observation scale and the mechanism of brittle creep as proposed.

6. Implications for Fault Mechanics

6.1. Link Between Crack Modes

[37] Several analogies can be drawn between our mode 1 fracture experiment and deformation processes in the crust. Tensile failure of natural materials occurs during dyke propagation and during secondary microcracking surrounding shear fractures. The mechanical process in our experiments is not limited to tensile fracture. The role of heterogeneities along a fault plane has similar consequences on the local values of the stress intensity factor (or energy release rate). An expression similar to equation (14) exists for mode 2 and mode 3 cracks when ignoring second-order coupling among shear modes [Gao *et al.*, 1991]. The only difference with the mode 1 expression is a constant coefficient dependent on the Poisson ratio. One could refer to Schmittbuhl *et al.* [2003a] for an extended discussion on the relation between rupture modes.

6.2. Importance of the Process Zone

[38] Fracture in rock samples or faults exhibit a process zone that encompasses a region with complex microcracking because of the high stress field around the crack tip. Significant energy is dissipated in the formation of the process zone and in the frictional work on these microcracks. This energy loss is much higher than the surface energy associated with the separation of the two blocks in contact. As the size of the process zone is observed to

increase with fault length, a scaling argument suggests that the energy release rate dissipated in the process zone also increases with the fault/system size [Scholz, 2002]. This results in an apparent scaling of the fracture energy with the system size, where the fracture energy includes all sources of energy dissipations [e.g., Abercrombie and Rice, 2005]. Our system does not involve a pronounced process zone because of the small bulk disorder. As a consequence, estimates of the fracture energy in our experiments are close to the surface energy, in contrast to earthquake data where the growth of the process zone and friction greatly influence the dissipation process. Our observations do not directly address the issue of the scaling of G_c with system size. The size of our system is fixed by the sample size (plate dimensions) and does not vary. The difference of fracture energy that we observe results from the change of the observation scale and not the sample scale.

6.3. Slow Slip Events

[39] Our observations provide a guide for understanding the simultaneous presence of acoustic emissions and smooth deformation during creep experiments in rock samples [e.g., Heap et al., 2009]. Such brittle creep behavior is possible due to the heterogeneous nature of the interface which produces, at the local scale, a complex pattern of ruptures (see Figure 10) because of elastic interactions. It is a competition between sites with subcritical or critical propagation (pseudo stick-slip crack advances) resulting in an average (macroscopic) steady deformation. This mode of rupture implies a variation of the fracture energy with observation scale. The fracture energy computed at the sample scale actually integrates all points along the front line and thus is an average among sites that are at $G = G_c$ (only a few points) and a majority of points that are pinned along the interface under unloading conditions with $G < G_c$. A higher proportion of sites along the front line are at $G = G_c$ when the loading speed is increased, and subsequently the crack speed. The difference between $\overline{G_c}$ and $\langle G_c \rangle$ vanishes when the speed of the crack approaches the Rayleigh wave speed. The deformation rate is an important factor that affects the large-scale estimate $\overline{G_c}$ while faintly modifying estimates at local scales. In the case of a dynamic crack, in our model, at a given time step, all points along the front line are moving. Our definition of the local fracture energy implies that at all time steps and for every position along front, the energy release rate is equal to the fracture energy. Averaging over all local estimates produces the exact same value as the macroscopic one $\overline{G_c} = \langle G_c \rangle$. Our results are more closely related to slow deformation processes occurring in the Earth crust rather than dynamic events, like creeping of fault segments, nucleation phase of earthquakes, postseismic slip or slow slip processes. The fracture energy for slow ruptures in the earth are lower (by few orders of magnitude) compared to values reported for dynamic fractures of the same size. This is the case for a creep event along the San Andreas fault reported by Rice and Simons [1976]. This is also suggested from the low slip to size ratio of slow events [e.g., Ide et al., 2007], which combined with Rice and Simons [1976, equation (67)] yields low values of fracture energy compared to regular earthquake. These studies however do not resolve the spatial distribution of fracture energy on the fault plane during the slow events which would make pos-

sible the comparison with macroscopic estimates as in our study.

7. Conclusion

[40] We provide a direct description of brittle creep crack propagation at different observational scales. At the local scale, the fracturing process is intermittent and is characterized by a complex fracture front morphology and a wide range of local crack velocities. At a given time, a mixture of slow and fast ruptures can be observed simultaneously. This complex pattern results from the presence of heterogeneities along the crack interface together with significant elastic interactions. When observed at the macroscopic scale, the variability of the local scales disappears and the crack propagation is smooth. This suggests that macroscopic observation of slow deformation processes (for example for rocks samples or faults) should be analyzed in the light of the heterogeneous nature of the material. Therefore, the fracture energy depends on the observation scale and its macroscopic estimate is lower than the average over local values.

[41] **Acknowledgments.** We gratefully acknowledge fruitful discussions with K.T. Tallakstad, V. Lazarus, N. Pindra, S. Santucci, S. Roux, J.P. Leblond, M. Bouchon, H. Karabulut, P. Meredith, P. Baud, and M. Heap and experimental support by Alain Steyer. This research is funded by ANR grant SUPNAF. J.E.E. was supported by a Caltech Seismological Laboratory fellowship. J.E.E. and J.P.A. were partially supported by the National Science Foundation (grant EAR-1015698). We thank Ian Main, the Associate Editor, and an anonymous reviewer for useful suggestions. Some figures were drawn with GMT software [Wessel and Smith, 1995].

References

- Abercrombie, R. E., and J. R. Rice (2005), Can observations of earthquake scaling constrain slip weakening?, *Geophys. J. Int.*, *162*, 406–424, doi:10.1111/j.1365-246X.2005.02579.x.
- Ampuero, J.-P., and A. M. Rubin (2008), Earthquake nucleation on rate and state faults: Aging and slip laws, *J. Geophys. Res.*, *113*, B01302, doi:10.1029/2007JB005082.
- Atkinson, B. K. (1984), Subcritical crack growth in geological materials, *J. Geophys. Res.*, *89*, 4077–4114, doi:10.1029/JB089iB06p04077.
- Atkinson, B. K., and P. G. Meredith (1987a), The theory of subcritical crack growth with applications to minerals and rocks, in *Fracture Mechanics of Rocks*, pp. 111–166, Academic, San Diego, Calif.
- Atkinson, B. K., and P. G. Meredith (1987b), Experimental fracture mechanics data for rocks and minerals, in *Fracture Mechanics of Rocks*, pp. 477–525, Academic, San Diego, Calif.
- Baud, P., and P. G. Meredith (1997), Damage accumulation during triaxial creep of Darley Dale sandstone from pore volumetry and acoustic emission, *Int. J. Rock Mech. Min. Sci.*, *34*(3–4), 24.e1–24.e10, doi:10.1016/S1365-1609(97)00060-9.
- Bean, C. J. (1996), On the cause of 1/f-power spectral scaling in borehole sonic logs, *Geophys. Res. Lett.*, *23*, 3119–3122, doi:10.1029/96GL02922.
- Blewitt, G. (2007), GPS and space-based geodetic methods, in *Treatise on Geophysics*, vol. 3, *Geodesy*, pp. 351–390, Elsevier, New York.
- Bouchon, M., H. Karabulut, M. Aktar, S. Ozalaybey, J. Schmittbuhl, and M.-P. Bouin (2011), Extended nucleation of the 1999 mw 7.6 Izmit earthquake, *Science*, *331*(6019), 877–880, doi:10.1126/science.1197341.
- Brace, W. F., and J. B. Walsh (1962), Some direct measurements of the surface energy of quartz and orthoclase, *Am. Mineral.*, *47*, 1111–1122.
- Das, S., and C. H. Scholz (1981), Theory of time-dependent rupture in the earth, *J. Geophys. Res.*, *86*, 6039–6051, doi:10.1029/JB086iB07p06039.
- Delaplace, A., J. Schmittbuhl, and K. J. Måløy (1999), High resolution description of a crack front in a heterogeneous plexiglas block, *Phys. Rev. E*, *60*, 1337–1343.
- Freiman, S. W. (1984), Effects of chemical environments on slow crack growth in glasses and ceramics, *J. Geophys. Res.*, *86*, 4072–4076.
- Gao, H., and J. R. Rice (1989), A first-order perturbation analysis of crack trapping by arrays of obstacles, *J. Appl. Mech.*, *56*, 828–836.

- Gao, H., J. R. Rice, and J. Lee (1991), Penetration of a quasi-statistically slipping crack into a seismogenic zone of heterogeneous fracture resistance, *J. Geophys. Res.*, *96*, 21,535–21,548.
- Grob, M., J. Schmittbuhl, R. Toussaint, L. Rivera, S. Santucci, and K. J. Måløy (2009), Quake catalogs from an optical monitoring of an interfacial crack propagation, *Pure Appl. Geophys.*, *166*, 777–799.
- Hansen, A., and J. Schmittbuhl (2003), Origin of the universal roughness exponent of brittle fracture surfaces: Stress-weighted percolation in the damage zone, *Phys. Rev. Lett.*, *90*, 045504, doi:10.1103/PhysRevLett.90.045504.
- Heap, M. J., P. Baud, P. G. Meredith, A. F. Bell, and I. G. Main (2009), Time-dependent brittle creep in Darley Dale sandstone, *J. Geophys. Res.*, *114*, B07203, doi:10.1029/2008JB006212.
- Ide, S., G. C. Beroza, D. R. Shelly, and T. Uchide (2007), A scaling law for slow earthquakes, *Nature*, *447*, 76–79, doi:10.1038/nature05780.
- Katsamanis, F. G., and C. G. Delides (1988), Fracture surface energy measurements of PMMA: A new experimental approach, *J. Phys. D Appl. Phys.*, *21*, 79–86, doi:10.1088/0022-3727/21/1/012.
- Lawn, B. R. (1975), An atomistic model of kinetic crack growth in brittle solids, *J. Mater. Sci.*, *10*, 469–480, doi:10.1007/BF00543692.
- Lawn, B. R. (1993), *Fracture of Brittle Solids*, Cambridge Univ. Press, New York.
- Lei, X., K. Kusunose, M. V. M. S. Rao, O. Nishizawa, and T. Satoh (2000), Quasi-static fault growth and cracking in homogeneous brittle rock under triaxial compression using acoustic emission monitoring, *J. Geophys. Res.*, *105*, 6127–6139, doi:10.1029/1999JB900385.
- Lengliné, O., and D. Marsan (2009), Inferring the coseismic and postseismic stress changes caused by the 2004 $m_w = 6$ Parkfield earthquake from variations of recurrence times of microearthquakes, *J. Geophys. Res.*, *114*, B10303, doi:10.1029/2008JB006118.
- Lockner, D. (1993), Room temperature creep in saturated granite, *J. Geophys. Res.*, *98*, 475–487, doi:10.1029/92JB01828.
- Måløy, K. J., S. Santucci, J. Schmittbuhl, and R. Toussaint (2006), Local waiting time fluctuations along a randomly pinned crack front, *Phys. Rev. Lett.*, *96*, 045501, doi:10.1103/PhysRevLett.96.045501.
- Okubo, P. G., and K. Aki (1987), Fractal geometry in the San Andreas fault system, *J. Geophys. Res.*, *92*, 345–356, doi:10.1029/JB092iB01p00345.
- Paterson, M. S., and T. Wong (2005), *Experimental Rock Deformation - The Brittle Field*, 2nd ed., Springer, New York.
- Rice, J. R., and D. A. Simons (1976), The stabilization of spreading shear faults by coupled deformation-diffusion effects in fluid-infiltrated porous materials, *J. Geophys. Res.*, *81*, 5322–5334, doi:10.1029/JB081i029p05322.
- Roux, S., D. Vandembroucq, and F. Hild (2003), Effective toughness of heterogeneous brittle materials, *Eur. J. Mech. Solids*, *22*, 743–749.
- Rubin, A. M. (1993), Tensile fracture of rock at high confining pressure: Implications for dike propagation, *J. Geophys. Res.*, *98*, 15,919–15,935.
- Santucci, S., M. Grob, R. Toussaint, J. Schmittbuhl, A. Hansen, and K. J. Måløy (2010), Fracture roughness scaling: A case study on planar cracks, *Europhys. Lett.*, *92*, 44001, doi:10.1209/0295-5075/92/44001.
- Schmittbuhl, J., and K. J. Måløy (1997), Direct observation of a self-affine crack propagation, *Phys. Rev. Lett.*, *78*, 3888–3891.
- Schmittbuhl, J., A. Delaplace, K. J. Måløy, H. Perfettini, and J.-P. Vilotte (2003a), Slow crack propagation and slip correlations, *Pure Appl. Geophys.*, *160*, 961–976.
- Schmittbuhl, J., A. Hansen, and G. G. Batrouni (2003b), Roughness of interfacial crack fronts: Stress-weighted percolation in the damage zone, *Phys. Rev. Lett.*, *90*, 045505, doi:10.1103/PhysRevLett.90.045505.
- Schmittbuhl, J., G. Chambon, A. Hansen, and M. Bouchon (2006), Are stress distributions along faults the signature of asperity squeeze?, *Geophys. Res. Lett.*, *33*, L13307, doi:10.1029/2006GL025952.
- Scholz, C. H. (1968a), Microfracturing and the inelastic deformation of rock in compression, *J. Geophys. Res.*, *73*, 1417–1432, doi:10.1029/JB073i004p01417.
- Scholz, C. H. (1968b), Mechanism of creep in brittle rock, *J. Geophys. Res.*, *73*, 3295–3302, doi:10.1029/JB073i010p03295.
- Scholz, C. H. (2002), *The Mechanics of Earthquakes and Faulting*, Cambridge Univ. Press, New York.
- Simons, M., and P. A. Rosen (2007), Interferometric synthetic aperture radar geodesy, in *Treatise on Geophysics*, vol. 3, *Geodesy*, pp. 391–446, Elsevier, New York.
- Titus, S. J., C. DeMets, and B. Tikoff (2006), Thirty-five-year creep rates for the creeping segment of the San Andreas Fault and the effects of the 2004 Parkfield earthquake: Constraints from alignment arrays, continuous global positioning system, and creepmeters, *Bull. Seismol. Soc. Am.*, *96*(4), S250–S268, doi:10.1785/0120050811.
- Wang, L., S. Hainzl, S. Ozeren, and Y. Ben-Zion (2010), Postseismic deformation induced by brittle rock damage of aftershocks, *J. Geophys. Res.*, *115*, B10422, doi:10.1029/2010JB007532.
- Wessel, P., and W. H. F. Smith (1995), New version of the generic mapping tools released, *Eos Trans. AGU*, *76*, 329–329, doi:10.1029/95EO00198.
- Wiederhorn, S. M., and L. H. Bolz (1970), Stress corrosion and static fatigue of glass, *J. Am. Ceram. Soc.*, *53*, 543–548, doi:10.1111/j.1151-2916.1970.tb15962.x.
- Wong, T. (1982), Shear fracture energy of westerly granite from postfailure behavior, *J. Geophys. Res.*, *87*, 990–1000.
- Zimmermann, R., and I. Main (2004), Hydromechanical behaviour of fractured rocks, in *Mechanics of Fluid-Saturated Rocks*, pp. 363–422, Elsevier, London.

J.-P. Ampuero and J. E. Elkhoury, Division of Geological and Planetary Sciences, California Institute of Technology, 1200 E. California Blvd., MC 252-21, Pasadena, CA 91125, USA. (ampuero@gps.caltech.edu; elkhoury@gps.caltech.edu)

O. Lengliné, J. Schmittbuhl, and R. Toussaint, Institut de Physique du Globe de Strasbourg, IPGS, UMR 7516, CNRS, Université de Strasbourg, 5 rue René Descartes, F-67084 Strasbourg, France. (olivier.lengline@eost-u.strasbg.fr; jean.schmittbuhl@eost-u.strasbg.fr; renaud.toussaint@eost-u.strasbg.fr)

K. J. Måløy, Department of Physics, University of Oslo, PB 1048, Blindern, N-0316 Oslo, Norway. (maloy@fys.uio.no)